Bulletin of the Seismological Society of America, Vol. 93, No. 1, pp. 264–282, February 2003

Stress-Breakdown Time and Slip-Weakening Distance Inferred from Slip-Velocity Functions on Earthquake Faults

by Takeshi Mikumo, Kim B. Olsen, Eiichi Fukuyama, and Yuji Yagi*

Abstract We estimate the critical slip-weakening distance on earthquake faults by using a new approach, which is independent of the estimate of fracture energy or radiated seismic energy. The approach is to find a physically based relation between the breakdown time of shear stress T_b, the time of peak slip-velocity T_{pv}, and the slip-weakening distance D_c, from the time histories of shear stress, slip, and slip velocity at each point on the fault, which can be obtained from dynamic rupture calculations using a simple slip-weakening friction law. Numerical calculations are carried out for a dynamic shear crack propagating either spontaneously or at a fixed rupture velocity on a vertical fault located in a 3D half-space and a more realistic horizontally layered structure, with finite-difference schemes. The results show that T_{pv} is well correlated with T_b for faults even with a heterogeneous stress-drop distribution, except at locations near strong barriers and the fault edges. We also investigate this relation for different types of slip-weakening behavior.

We have applied the method to two recent, strike-slip earthquakes in western Japan, the 2000 Tottori and the 1995 Kobe events. We integrated the slip-velocity functions on the vertical fault obtained from kinematic waveform inversion of strong-motion and teleseismic records from the arrival time of rupture T_r to the time of the peak-slip velocity T_{pv}, and we then corrected the slip obtained at T_{pv} for the errors expected from the dynamic calculations. It was found that the slip-weakening distance D_c estimated in the frequency window between 0.05 and 0.5 Hz ranges between 40 and 90 cm on the two earthquake faults. However, if we consider the limited frequency resolution of the observed waveforms, probable time errors in the slip-velocity functions obtained from kinematic inversion, and the uncertainty of the slip-weakening behavior, the above estimates may be those located between the minimum resolvable limit and the upper bound of their real values. The estimated D_c values do not necessarily seem to indicate larger values in the shallower part and smaller values in the deeper part of the fault, but rather a spatially heterogeneous distribution that appears to be dependent on the local maximum slip. This possible dependence might be interpreted by the frictional properties of the fault such as the degree of roughness or the thickness of gouge layers, in addition to stress heterogeneities.

Introduction

It is now widely accepted that the earthquake source can be modeled by shear rupture propagating on a pre-existing or newly created fault embedded in the earth's crust or upper mantle. The rupture is thought to initiate quasi-statically at a small nucleation zone and then develop into an unstable, dynamic phase over the fault plane. The rupture process may be controlled not only by the stress distribution on and around the fault zone but also by the frictional properties of the fault surface. An increasing number of studies have recognized that the constitutive relation on the fault, particularly the slip-dependent weakening of shear stress, plays a critical role in the dynamic part of the rupture process and hence on strong ground motions during large earthquakes.

The concept of slip-weakening behavior was first introduced by Ida (1972) and Palmer and Rice (1973) into shear crack models to remove the well-known mathematical singularity at the propagating crack tip, by assuming the existence of a cohesive zone just behind the rupture front. Al-

*Present address: Institute of Seismology and Earthquake Engineering, Building Research Institute, Tsukuba, Ibaraki 305-0802, Japan; *yagi@kenken.go.jp.*

though Ida (1972) assumed several types of behavior, it was idealized by Andrews (1976a,b) as a simple slip-weakening model, as shown in Figure 1, where the initial stress σ_0 at each point on a 2D fault increases up to the yield stress σ_y as the rupture front approaches, and then decreases linearly with ongoing slip to the residual friction or dynamic friction level σ_f. The slip at σ_f is defined as the critical weakening slip or slip-weakening distance D_c, and the effective surface energy G to be the work done is defined as fracture energy $G = (\sigma_y - \sigma_f) D_c/2$. This model was extended by Day (1982) into the fault in a 3D homogeneous whole-space and later applied in a number of theoretical studies and dynamic numerical simulations using various frictional conditions (e.g., Ohnaka and Yamashita, 1989; Matsu'ura *et al.*, 1992; Shibazaki and Matsu'ura, 1992, 1998; Fukuyama and Madariaga, 1995, 1998, 2000; Tullis, 1996; Madariaga *et al.*, 1998; Madariaga and Olsen, 2000; Campillo *et al.*, 2001). Among these studies, Ohnaka and Yamashita (1989) proposed a slip-weakening behavior based on laboratory experiments, whereas Matsu'ura *et al.* (1992) presented several slip-strengthening and slip-weakening relations based on a physical model that was derived from frictional resistance due to microscopic interactions between statistically self-similar fault surfaces with different wavelength of roughness. Campillo *et al.* (2001) also provided effective slip-weakening laws for heterogeneous fault surfaces with several barriers.

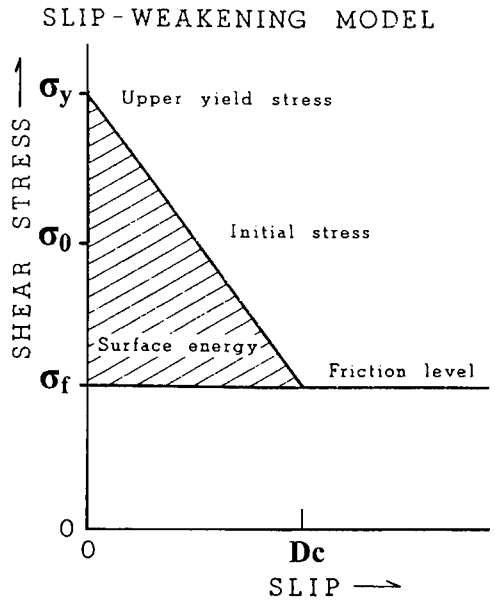

Figure 1. Linear slip-weakening friction law, modified from Andrews (1976a,b). σ_y, yield stress; σ_0, initial stress; σ_f, residual frictional stress; D_c, critical slip-weakening distance.

These conceptual models of slip weakening are now supported by experimental evidence on rock materials (e.g., Dieterich, 1981; Okubo and Dieterich, 1984; Ohnaka *et al.*, 1987; Scholz, 1988; Ohnaka and Kuwahara, 1990; Dieterich and Kilgore, 1996; Ohnaka, 1996; Ohnaka and Shen, 1999). Some of these laboratory experiments (Dieterich, 1981; Ohnaka and Kuwahara, 1990) provided the time histories of stress, slip, and slip velocity, depicting the breakdown time of stress with the order of 1/10 msec and the corresponding D_c in the range from a few to several μm. Another important finding from the experiments is that D_c is closely related to the characteristic wavelength of the roughness of the fault surface (Ohnaka and Kuwahara, 1990; Ohnaka and Shen, 1999) and also controlled by the thickness of fault gouge layers (Marone and Kilgore, 1993). On the other hand, another class of a rate- and state-dependent friction law was proposed by Dieterich (1979, 1981) and Ruina (1993), based on extremely low slip-rate experiments on frictional sliding. Although this friction law will dominate at an early stage of the quasi-static process in a nucleation zone (e.g., Dieterich and Kilgore, 1996), at a stress recovery process on the fault and during the earthquake cycle, the dynamic rupture process with much higher slip velocities may not be controlled by this law but rather by the slip-dependent behavior (e.g., Okubo and Dieterich, 1984; Kato and Tullis, 2001).

For actual earthquakes, several attempts have been made to date to infer the slip-weakening distance D_c. An earlier study of Papageorgiou and Aki (1983) estimated D_c to be in the range between 40 and 400 cm from acceleration spectra for several California earthquakes on the basis of their specific barrier model, although these estimates were later refined to the range from 20 to 150 cm (Aki and Papageorgiou, 1987). More recently, Ide and Takeo (1997) used the results from kinematic waveform inversion of strong-motion records obtained during the 1995 Kobe earthquake and found that D_c ranges between 50 and 100 cm for deeper fault sections and between 100 and 150 cm for shallower fault sections. Olsen *et al.* (1997) and Peyrat *et al.* (2001) also found D_c on the order of 80 cm from waveform inversion of the accelerograms observed during the 1992 Landers earthquake, with spontaneous dynamic rupture models. Day *et al.* (1998) also calculated the time histories of dynamic shear stress change on the fault, from kinematic slip models of three recent earthquakes, but the stress change was rather gradual, probably due to the limited resolution in the underlying kinematic inversions. On the other hand, Guatteri and Spudich (2000) claimed that strong-motion waveforms from the 1979 Imperial Valley earthquake could not resolve two rupture models having similar fracture energy, with $D_c = 30$ cm and high strength excess and with $D_c = 100$ cm and low strength excess, in the 0- to 1.6-Hz frequency range. Pulido and Irikura (2000) used the spatio-temporal distribution of apparent stress calculated from slip-velocity functions on the fault and estimated D_c to range between 100 and 350 cm for the 1992 Landers earthquake. Ohnaka (2000) calculated D_c from a relation between the critical size of the nucleation zone and the breakdown stress drop mainly for the observed data of slow initial phase given by Ellsworth and Beroza (1995) for a number of earthquakes

with different magnitudes, their values ranging between 1 and 300 cm.

It seems, however, that some of the D_c values may be overestimated due to limited data resolution and may furthermore be biased by computational constraints, although we believe that D_c may be a significant fraction of the maximum slip on the fault. There also remains a question as to what extent D_c scales with the size of the fault zone and hence with the earthquake size (Marone and Kilgore, 1993), whereas its scale effect has been suggested for natural faults (Scholz and Aviles, 1986), from laboratory experiments (Okubo and Dieterich, 1984; Ohnaka and Shen, 1999), and from synthetic data (Ohnaka, 2000).

In the present study, we use a simple, new approach to estimate the slip-weakening distance D_c from strong-motion records, independently from the estimate of the fracture energy or radiated seismic energy. The motivation of our method comes from the time histories of stress, slip, and slip velocity obtained in laboratory experiments (Dieterich, 1981; Ohnaka and Kuwahara, 1990), suggesting that the first pulse width of slip acceleration on the fault surface is closely related to the local stress breakdown time (Ohnaka and Yamashita, 1989; Shibazaki and Matsu'ura, 1998). Another motivation is the clearly different shapes of the slip-velocity time histories on the fault for different slip-weakening distances (Guatteri and Spudich, 2000). As we will mention later, our method requires high resolution in the time domain both in the kinematic and dynamic slip-velocity functions on the fault. We apply this method to estimate D_c in the frequency range between 0.05 and 0.5 Hz for two recent, vertical strike-slip earthquakes, that is, the 2000 Tottori and 1995 Kobe earthquakes in western Japan.

Dynamic Rupture Modeling

In order to estimate the slip-weakening distance D_c on actual earthquake faults, we perform, as a first step, numerical experiments for dynamic shear cracks propagating either spontaneously or at a fixed rupture velocity on a vertical fault located in a 3D half-space or a more realistic horizontally layered structure. From these calculations under various conditions, we find a physically based relation between the breakdown time of shear stress T_b, the time of peak slip-velocity T_{pv}, and the prescribed slip-weakening distance D_c, at each point on the 2D fault. T_b is the time when the shear stress drops to the level of the residual frictional stress, at which the ongoing slip reaches D_c, but cannot be directly inferred from seismic observations. Instead, T_{pv} should, in principle, be slightly different from T_b, and it is, on the other hand, an observable parameter. The slip at T_{pv} is denoted here as D_c'. Based on such a relation, it is possible to use T_{pv} observed from kinematic waveform inversion of strong-motion records from an earthquake in order to estimate D_c after correcting T_{pv} for T_b. For this purpose, we solve the 3D elastodynamic equations using appropriate boundary conditions with finite-difference schemes, as described in a following section.

Theoretical Considerations

The validity of our method may be justified from the theoretical background (Fukuyama *et al.*, 2002) described below. The shear traction on a 2D fault in a homogeneous elastic medium has been expressed by Fukuyama and Madariaga (1998) using boundary integral equations in the following form,

$$\sigma\,(x_1,x_2,t) \;=\; -\mu V(x_1,x_2,t)/2\beta + \int_S\int_0^t K\,(x_1,x_2,t|\xi_1,\xi_2,\tau)\;V\,(\xi_1,\xi_2,\tau)\;d\tau\;d\xi_1\;d\xi_2 \quad (1)$$

where σ and V are the shear stress and slip velocity, K is the kernel related to the slip history, μ and β are the rigidity and shear-wave velocity in the medium, respectively. A more detailed expression of K is given by Fukuyama and Madariaga (1998). The first term is proportional to the current slip velocity, whereas the second term is the contribution from the past slip history in space and time. When the total stress σ drops to the level of the residual stress at T_b, and if the second term changes smoothly around this time, then we expect that the slip velocity in the first term would reach its peak at that time. Figure 2 shows one of numerical examples of the calculated stress history (Fukuyama *et al.*, 2002) for the linear slip-weakening behavior as given by Andrews (1976a,b), near the center of a fault with a dimension of 25.6 km × 12.8 km, being subjected to a uniform stress drop of 3.5 MPa and a prescribed slip-weakening distance of D_c = 70 cm. As expected, the contribution from the sec-

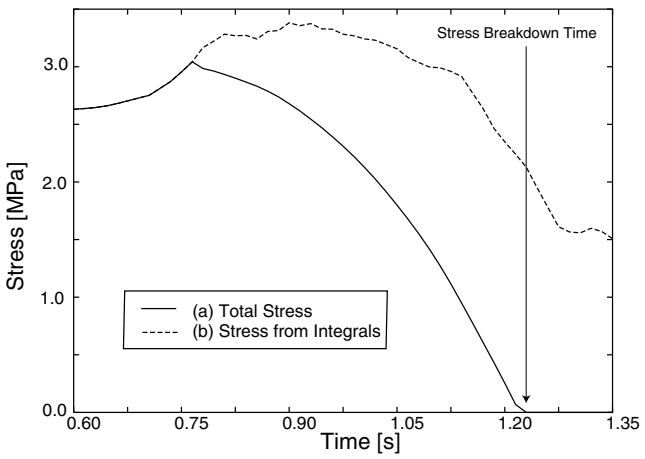

Figure 2. Time history of stress changes near the center of a homogeneous fault subjected to a uniform stress drop of 3.5 MPa and D_c = 70 cm. The fault dimension is 25.6 km × 12.8 km with a grid size of 0.2 km × 0.2 km, and the time increment is taken as 0.015 sec, in this calculation. (a) Total stress, (b) stress contribution from past slip in space and time (Fukuyama *et al.*, 2002).

ond term changes smoothly around the breakdown time $T_b \sim 1.22$ sec of the total stress σ, indicating that our technique should work well at this point.

However, if the integral term changes rapidly near the edges of the fault or near strong barriers, where a stopping phase will be generated due to abrupt change in the rupture velocity, the time of peak slip-velocity T_{pv} will deviate from T_b to some extent. Fukuyama *et al.* (2002) provided several examples of the time histories of the stress, slip velocity, and slip calculated from dynamic rupture propagating on a fault with barriers and asperities and concluded that the present technique works properly except for the case in front of strong barriers.

Method of Numerical Calculations

First, we simulate a dynamic shear crack on a vertical fault in a 3D homogeneous half-space (Miyatake, 1980) and in a horizontally layered structure (Mikumo *et al.*, 1987; Mikumo and Miyatake, 1995), which is subjected to the shear stress working parallel to the strike direction. The dynamic rupture propagation over the vertical fault can be calculated by solving the elastodynamic equation, incorporating the slip-weakening friction together with appropriate boundary conditions. The slip-weakening condition introduced here is

$$\sigma(D) = \sigma_y - (\sigma_y - \sigma_f)\, D/D_c \text{ for } D < D_c, \quad \text{and} \quad \sigma(D) = \sigma_f \text{ for } D > D_c \qquad (2a)$$

for $\sigma_f < \sigma_0 < \sigma_y$, following Andrews (1976a,b), where D is the current slip displacement. The stress change for $D < D_c$ relative to the initial stress σ_0 may also be written as

$$\Delta\sigma(D) = (\sigma_y - \sigma_0)\,(1 - D/D_c) - (\sigma_0 - \sigma_f)\, D/D_c, \qquad (2b)$$

where $\sigma_y - \sigma_0$ is called the strength excess, and $\sigma_0 - \sigma_f$ is the dynamic stress drop. The boundary conditions imposed here are (1) the continuity of the normal stress and normal displacement across the vertical fault, (2) traction-free vertical stress at the ground surface, (3) the continuity of all stress and displacement components at each of the layer interfaces in case of a horizontally layered structure (Mikumo *et al.*, 1987), and (4) absorbing boundary conditions at the sides and bottom of the model space (Clayton and Engquist, 1977). The radius of the nucleation zone for dynamic rupture in the 3D case is given as

$$R_c = (7\pi/24)\mu D_c\, (\sigma_y - \sigma_f)/(\sigma_0 - \sigma_f)^2 \qquad (3)$$

(Day, 1982). To initiate dynamic rupture, the initial stress is taken as σ_f or a small preslip is prescribed within this zone. The rupture is assumed to propagate at a fixed velocity equivalent to 70% of the *S*-wave velocity in each layer, in second-order finite difference calculations. This case is referred to as a quasi-dynamic rupture.

We also solve our problem by a fourth-order staggered-grid finite difference scheme for spontaneous rupture propagation, which was first introduced by Madariaga (1976) and later developed by Virieux (1986), Levander (1988), and particularly by Olsen (1994), Olsen *et al.* (1995), Olsen and Archuleta (1996), and Madariaga *et al.* (1998). This scheme solves the 3D elastodynamic equations through the velocity–stress formulations, using a fourth-order approximation to spatial derivatives and a second-order approximation to time derivatives. In this scheme, stresses and velocities are computed at alternating half-integer time step and at half-integer grid spacing but have appropriate symmetries with respect to the fault plane (Madariaga *et al.*, 1998). A free-surface boundary condition is included at the top and sponge layers, in addition to absorbing boundary condition at the remaining grid boundaries (Madariaga *et al.*, 1998). This method also incorporates the slip-weakening friction law given in equation (2), where σ_f is taken to be 0 for simplicity. Dynamic rupture is initiated by reducing the yield stress σ_y to 0 in the nucleation zone around the hypocenter, followed by spontaneous propagation. The numerical and dynamic parameters used in the second- and fourth-order finite-difference calculations are listed in Table 1, and the crust and upper-mantle velocity structures adopted here are listed in Tables 2 and 3.

Numerical Results for a Homogeneous Fault

We tested our method for a uniformly loaded vertical fault in a homogeneous medium using the quasi-dynamic finite-difference scheme. The slip-weakening distance was 20 cm, and the prescribed stress drop was 2 MPa. Figure 3 shows a typical behavior of the time histories of shear stress, slip, and slip velocity at a location on the fault. It should be noticed that the slip and slip velocity start to evolve as the shear stress increases due to the arrival of the rupture front and that the slip velocity rapidly increases as the stress drops from its yield value and then reaches the peak value at time T_{pv}. However, T_{pv} deviates slightly from the stress-breakdown time T_b, and the slip D_c' at time T_{pv} is somewhat different from the prescribed slip-weakening distance D_c at time T_b.

The calculations show that the slip D_c' at time T_{pv} at a number of selected points on the fault scatters between 14 and 26 cm around the prescribed value of 20 cm (not shown here), suggesting that the slip-weakening distance in this case can be recovered with an error of less than 30% from the measurement of the time of the peak slip-velocity. The rather large deviations arise mainly from the points closer to the edges of the fault. For heterogeneous cases, we will show similar test results in the section $T_b - T_{pv} - D_c'$ Relations for two models (Figs. 4, 5) for the Tottori earthquake.

Application to Two Strike-Slip Earthquakes

Now, we apply our method to two recent, strike-slip earthquakes that occurred on near-vertical faults in order to

Table 1
Parameters for 3D Dynamic Modeling

		1*	2†
Model dimension	(km)	46 × 35 × 25	100 × 90 × 50/120 × 80 × 50
Grid spacing	(km)	0.25	1.0/0.5
Time increment	(sec)	0.0125	0.05/0.025
Fault dimension	(km)	25 × 15 (0–15)	24 × 15 (1–16)
Yield stress	(MPa)	10	(estimated)
D_c (prescribed)	(cm)	20, 30, 70	10, 20, 30, 40
Rupture velocity		(spontaneous)	0.70 β

*Spontaneous dynamic rupture calculations with a fourth-order staggered-grid finite-difference scheme.
†Quasi-dynamic rupture calculations with a second-order finite-difference scheme. Numerals in parentheses indicate the fault depth range, β is the *S*-wave velocity, V_s, in each layer (Table 2).

Table 2
Crustal Structure for the Tottori Region* Used in the Dynamic Rupture Calculations with Yagi's (2001) Model

Layer No.	H (km)	V_p (km/sec)	V_s (km/sec)	ρ (g/cm^3)
1	0	5.50	3.18	2.68
2	2	6.05	3.50	2.80
3	17	6.60	3.82	2.90
4	32	8.00	4.02	3.20

*Shibutani *et al.* (2001).

Table 3
Crustal Structure for the Tottori Region Used in the Dynamic Calculations with the Fukuyama–Dreger Model

Layer No.	H (km)	V_p (km/sec)	V_s (km/sec)	ρ (g/cm^3)
1	0	5.50	3.14	2.30
2	3	6.00	3.55	2.40

H, depth to top of layer; V_p, *P*-wave velocity; V_s, *S*-wave velocity; ρ, density.

evaluate the slip-weakening distance using the distributions of fault slip and stress change derived primarily from strong ground motions recorded at near-source stations.

The 2000 Tottori Earthquake

The Tottori earthquake (M_w 6.6) occurred in the western Tottori region, western Honshu, Japan, on 6 October 2000. The hypocenter of the mainshock was located at 35.27° N and 133.35° E at a depth of 11 km (Japan Meterological Agency, [JMA]). The centroid moment tensor (CMT) solutions from regional data and the focal mechanism solution from local data consistently provided a purely strike-slip mechanism for this earthquake (Fukuyama *et al.*, 2001; Shibutani *et al.*, 2001). Observations from local high-resolution stations revealed that many aftershocks were distributed over a length of about 25–30 km in the N27°–30°W direction at depths between 1 and 15 km (Shibutani *et al.*, 2001), although this distribution was extended some days later toward the northwest direction, and a separate group of aftershocks occurred about 25 km westward in a direction parallel to the main distribution. This direction agrees with the strike of one of the nodal planes determined from the CMT solutions.

The mainshock has been well recorded at a number of near-source strong-motion stations, the K-NET and KiK-net operated by the National Research Institute for Earth Sciences and Disaster Prevention (NIED), regional broadband stations, and teleseismic stations. Until now, three different source models have been obtained from kinematic inversion: by E. Fukuyama and D. S. Dreger (unpublished manuscript, 2001) from regional broadband seismic waveforms, by Yagi (2001) from near-source strong-motion data and teleseismic waveforms, and by Iwata and Sekiguchi (2001) from near-source strong-motion records and Global Positioning System (GPS) and leveling data. In our study, we refer to Yagi's (2001) slip model to estimate the dynamic parameters, with some reference to the models of Fukuyama and Dreger (2001) and Iwata and Sekiguchi (2001).

$T_b - T_{pv} - D_c'$ Relations

We have made calculations for the T_b–T_{pv}–D_c' relations for the following two models, both of which include non-uniform slip distributions and hence heterogeneous stress drop (not shown here). One of the quasi-dynamic calculations is for an early version of Yagi's (2001) model (version 0) with $D_c = 30$ cm for a fault with a dimension of 24 km × 16 km located in the layered velocity structure defined in Table 2. Comparing the time histories of stress, slip, and slip velocity (not shown) with those for the homogeneous fault, the shear stress drops rather rapidly and the slip-velocity functions yield narrower pulse widths. This can be explained by short scale-length, stress-drop heterogeneities, as has been pointed out by Beroza and Mikumo (1996). Figure 4 shows the $T_b - T_{pv}$ relation at the right-hand side and the $T_{pv} - D_c'$ relation at the left-hand side for several selected points aligned in the strike and dip directions from the rupture starting point. In this case D_c' falls between 20 and 38 cm except for one point, suggesting that the slip-weakening distance may be recovered again with an error of 30%.

For comparison, we also estimated the T_b–T_{pv}–D_c' relation for the Fukuyama and Dreger's model (2001), which includes a vertical fault with a dimension of 25 km × 15

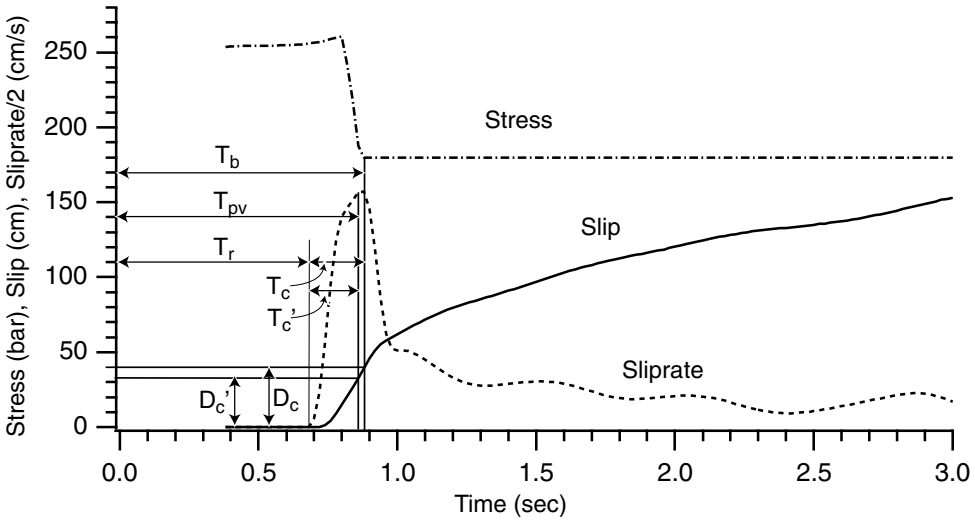

Figure 3. A typical behavior of the time history of shear stress, slip, and slip velocity on the fault. T_b, breakdown time of stress; T_{pv}, time of peak slip-velocity; D_c, slip at time T_b; D_c', slip at time T_{pv}.

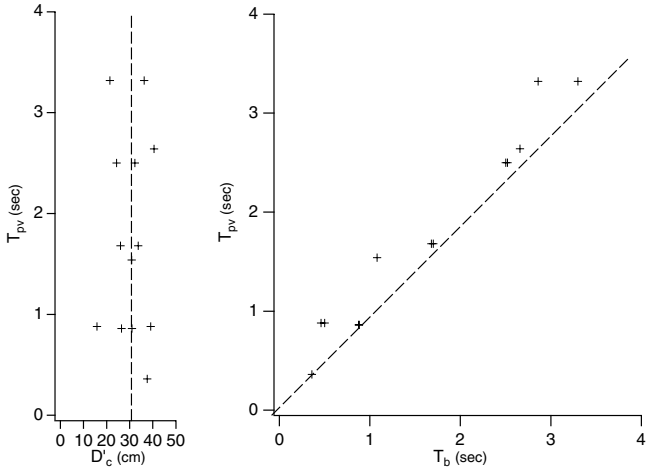

Figure 4. Relation between T_{pv} and T_b (right) and between D_c' and T_{pv} (left) for a heterogeneous fault with a prescribed value of D_c = 30 cm in Yagi's preliminary slip model (2001) for the Tottori earthquake. T_b and T_{pv} are measured from the time at the rupture starting point.

km located in the velocity structure listed in Table 3. The fault is subjected to a yield stress of 10MPa, a prescribed slip-weakening distance of 70 cm, and an assumed tectonic stress of 4.25 MPa. The rupture was started artificially at a depth of 11 km in the middle of the fault length. Figure 5 shows the relations between T_b and T_{pv} and between T_{pv} and D_c' for 49 points nearly evenly distributed on the fault, calculated from the stress, slip, and slip-velocity functions obtained by a fourth-order accurate finite-difference method. We see that T_{pv} in this case is very well correlated with T_b. D_c' estimated from T_{pv} ranges between 63 and 85 cm, indicating that the slip-weakening distance can be retrieved within an error of 17%. The deviation of D_c' exceeding 10% comes from several points near the upper fault edge and near the bottom corners of the fault. Later in this section, we will show the $T_b - T_{pv} - D_c'$ relations for the Yagi's final model (version 1).

Slip Distribution from Kinematic Waveform Inversion (Yagi's Model Version 1)

Figure 6 shows the horizontal projection of the fault traces on the ground, the fault-plane solutions, and the distribution of near-source stations. Yagi (2001) carried out kinematic waveform inversion of 17 strong-motion records from the 6 K-NET stations (Kinoshita, 1998) shown here and 10 *P*-wave records from 10 teleseismic stations. The strong-motion data were bandpassed between 0.05 and 0.5 Hz and numerically integrated to ground velocity with a sampling time of 0.25 sec, whereas the teleseismic data were bandpassed between 0.01 and 0.8 Hz and converted to ground displacement with a sampling time of 0.25 sec. The frequency range has been adopted to remove low-frequency noise arising from the integration procedure and also because the Green's function is not known well enough at frequencies above 0.5 Hz. We used a fourth-order butterworth filter. Yagi (2001) estimated the detailed spatiotemporal distribution of fault slip using a multi–time window inversion to all the data. For this inversion, the entire fault was divided into three segments, with 21 subfaults for FD1, 70 subfaults for FD2, and 14 subfaults for FD3, with dimensions of each subfault of 2 km × 2 km. The Green's functions for all subfault to strong-motion station pairs were calculated by the discrete wavenumber method developed by Koketsu (1985), while the functions for teleseismic stations were calculated by the method of Kikuchi and Kanamori (1991). The velocity structures used here are given in Tables 2 and 4,

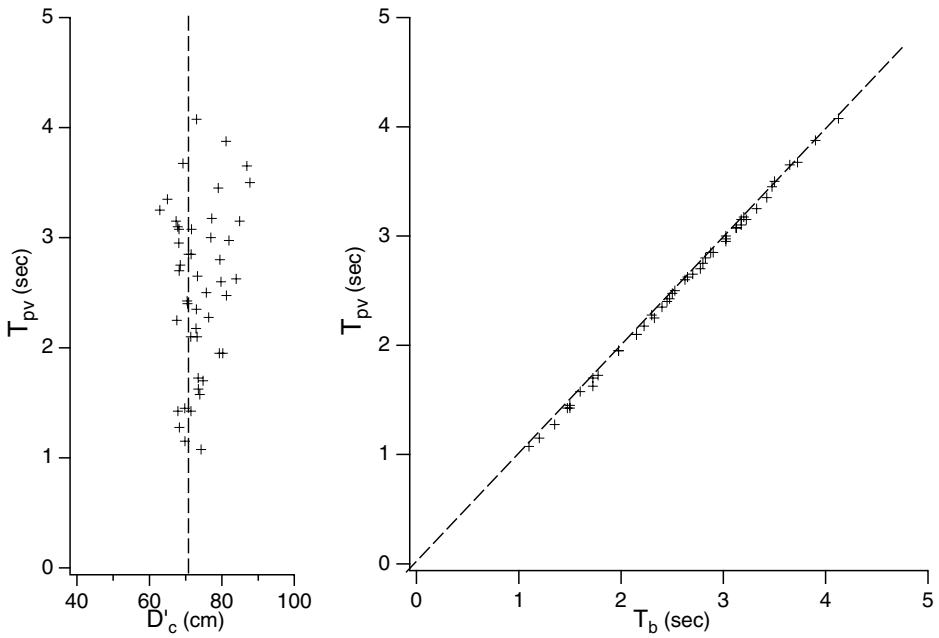

Figure 5. Same as Figure 3, but for a prescribed value of $D_c = 70$ cm in Fukuyama and Dreger's slip model (2001).

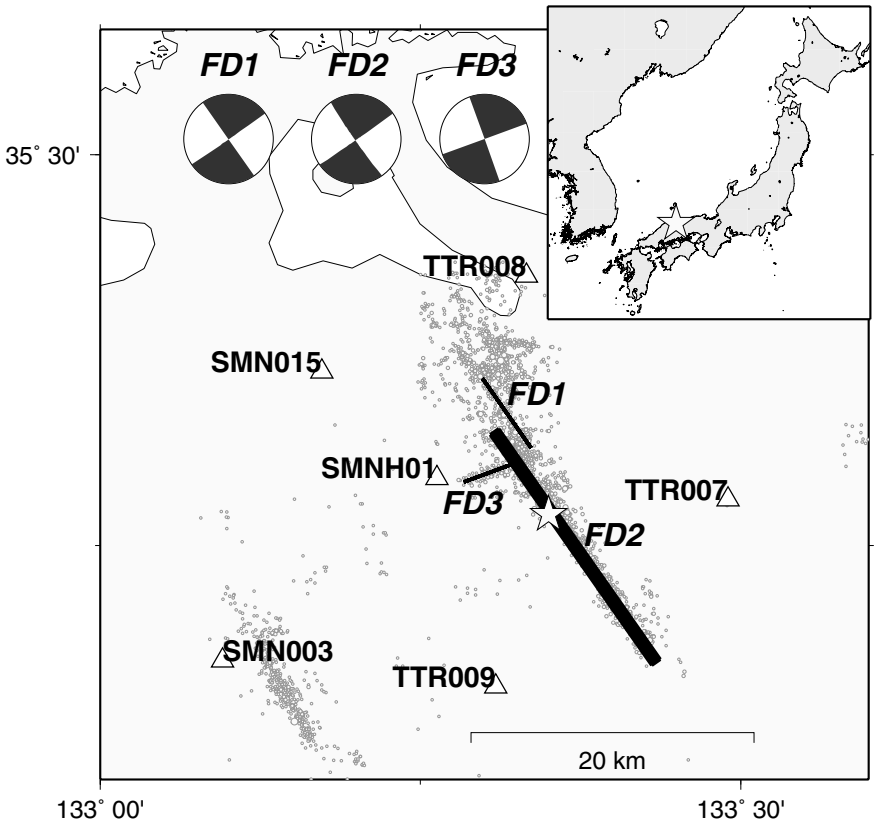

Figure 6. Location of the 2000 Tottori earthquake with the horizontal projection of three fault traces FD1, FD2, and FD3 inferred from the aftershock distribution, fault-plane solutions, and near-source strong-motion stations (NIED).

Table 4
Crust and Upper Mantle Structure Used for Teleseismic Receiver Stations (Yagi, 2001)

Layer No.	H (km)	V_p (km/sec)	V_s (km/sec)	ρ (gr/cm^3)
1	0	5.57	3.36	2.65
2	15	6.50	3.74	2.87
3	33	8.10	4.68	3.30

For Green's functions, the attenuation terms are included with T/Q_p = 1.0 (sec) and T/Q_s = 4.0 (sec).

where we refer to Table 2 for near-source regions and Table 4 for the teleseismic receiver stations. The basis source time function on each subfault is expanded in 39 sequential overlapping triangles, each having a half duration of 0.25 sec with a time shift of 0.25 sec, and resampled at an interval of 0.05 sec. To allow all subfaults to slip at any time, the start time of the source time function at all subfaults is set to 0 sec. All the observed records used here and the corresponding synthetic waveforms obtained from the final inversion are compared in Figure 7, generally showing a very good fit. Figure 8a shows a smoothed slip distribution on the two segments FD1 and FD2, which has been obtained from the final inversion. The slip on the southernmost subfault of FD1 and the northernmost subfault of FD2, which are parallel and partly overlap, are superimposed, and the segment FD3 is omitted. The maximum slip in the central fault section at a depth of about 6 km above the hypocenter reaches 2.3 m, and the large values of slip exceeding 1.5 m are confined mainly in the upper fault section at depths between 3 and 9 km along strike distances between 6 and 21 km.

Spatial Distribution of Stress Changes

Next, we calculate the spatial distribution of static stress change from the slip distribution shown in Figure 8a. The procedure follows the approach of Miyatake (1992) and Mikumo and Miyatake (1995). In this approach, local static stress changes at each point are derived by solving the static equilibrium equations in the 3D space, combined with the boundary conditions described in the section Dynamic Rupture Modeling. Given these static stress changes, we first calculate the slip from the dynamic rupture propagation and then take the ratio between the kinematic and dynamic slip at each point on the fault. The ratio is multiplied to the previously obtained static stress drop, and this procedure is repeated in an iterative, least-squares fashion until the root-mean-square (rms) difference between the kinematic and dynamic slip over the fault is minimized. For practical reasons, we interpolate the kinematic slip calculated at every 2 km × 2 km subfaults (Fig. 8a) into 0.5 km × 0.5 km subfaults.

Figure 8b shows the spatial distribution of the calculated stress change. The maximum static stress drop corresponding to the maximum slip reaches 90 bars (9 MPa), and the stress drop in the zones of slip larger than 1.5 m is about 30 bars (3 MPa). At middepths near the west-northwest fault section and around the east-southeast fault edge and the shallowest section, there are zones of negative stress drop (stress increase). Thus, the stress change on the fault was found to be quite heterogeneous.

Estimate of D_c from the Slip-Velocity Functions

Figure 9 shows the slip-velocity time functions on all subfaults of the segment FD2, which were obtained at every 0.05 sec in the final inversion to match the synthetics to the recorded waveforms. In order to estimate the slip-weakening distance through the procedure described in the foregoing sections, we numerically integrate the slip-velocity time functions from the time of the rupture arrival T_r to the time of the peak slip-velocity T_{pv} on each subfault, where T_r has been estimated within an error of 0.25 sec from the inversion. The calculations are made only for selected slip-velocity functions that arrive at the time T_r and are not contaminated by minor spurious oscillations. The integration procedure provides D_c' at time T_{pv}. The estimated values of D_c' are listed on the top of the slip-velocity function in each subfault in Figure 9.

To estimate the actual slip-weakening distance D_c from D_c', we made dynamic calculations with the spontaneous rupture finite-difference scheme for the heterogeneous fault, using the final slip and the stress change shown in Figure 8a and b as the observational constraints. For practical reasons, we interpolated the spatial distributions into a grid spacing of 0.25 km. The calculations were made for selected points (a, b, c, d, m, and n), for prescribed values of D_c = 30 cm and D_c = 70 cm. Figure 10 shows an example of the calculated time histories of stress change, slip, and slip velocity at points b and m. It is clear that for the case of D_c = 70 cm the stress drops more slowly and it takes a longer time for the slip rate to reach its peak than for the case of D_c = 30 cm. Figure 11 shows the deviations of T_{pv} from T_b and those of D_c' from the prescribed values of D_c for the six selected points, where large slip-velocities have been obtained. From these results we find that correction factors D_c/D_c' to be applied to the observed D_c' values are (a) 1.08, (b) 0.96, (c) 0.96, (d) 1.00, (m) 1.00, and (n) 1.25. These factors differ from unity in less than 10% except for point n and are rather small as compared with the uncertainty described in the next section.

Resolution of the Estimated D_c Values

The resolution of D_c depends on the resolvable frequency involved in the observed records and also on how accurately T_{pv} can be estimated from these records. The resolution of T_{pv} is restricted by the bandwidth of the observed records and also by the sampling time interval of the calculated slip-velocity functions used in the kinematic inversion. As a first step, we estimate its minimum resolvable value D_{cmin} tentatively following Guatteri and Spudich's expression (2000), which gives $D_{cmin} = V_{av}\, T_{cmin}$, where T_{cmin} is taken as the shortest modeled period involved in the ob-

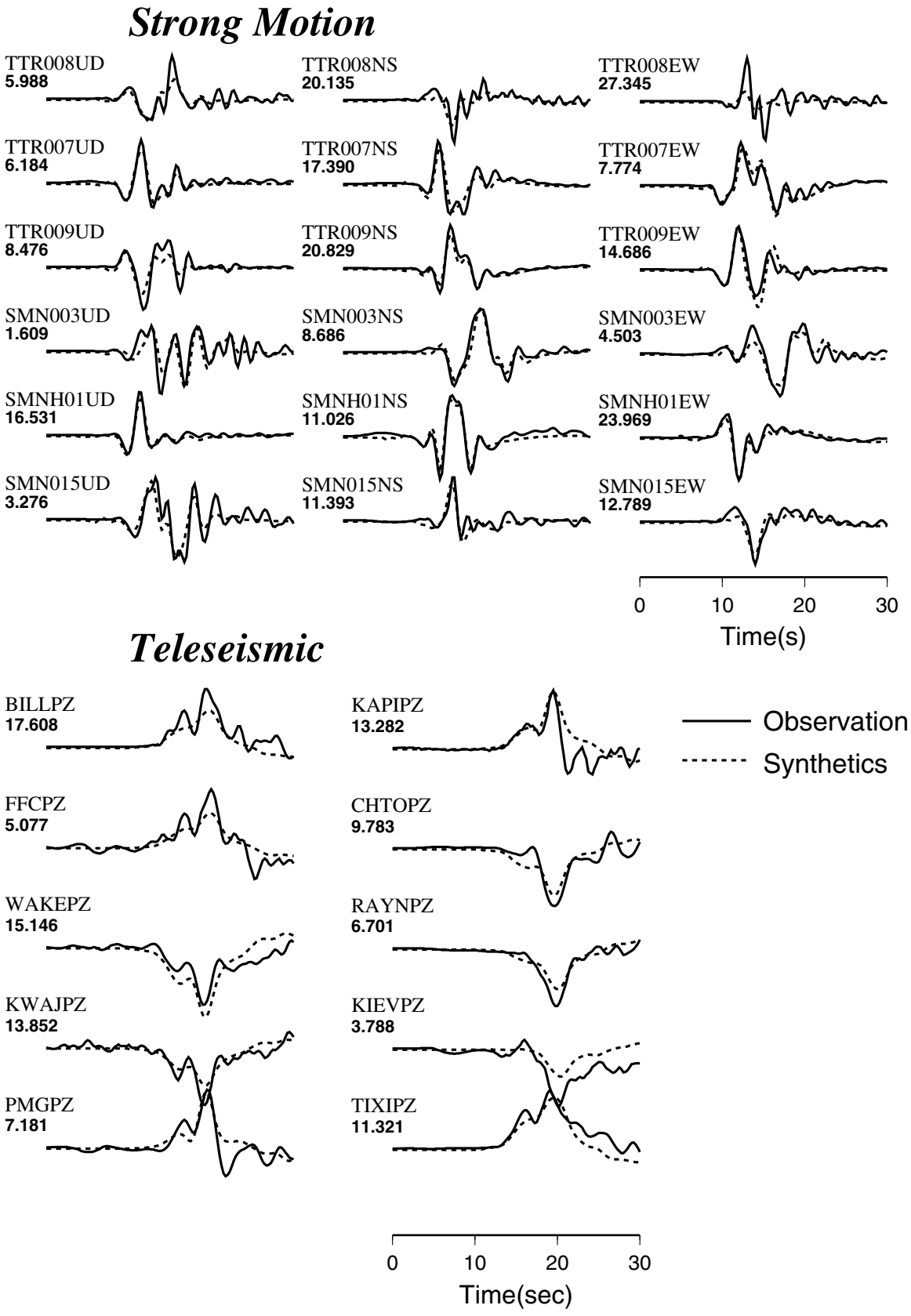

Figure 7. Strong-motion velocity waveforms recorded at near-source stations and *P*-wave displacement waveforms recorded at teleseismic stations, along with the corresponding synthetic waveforms obtained from kinematic inversion (Yagi, 2001). The waveforms are indicated by the station code and the component with the epicentral distance (in km for strong-motion stations and in degrees for teleseismic stations).

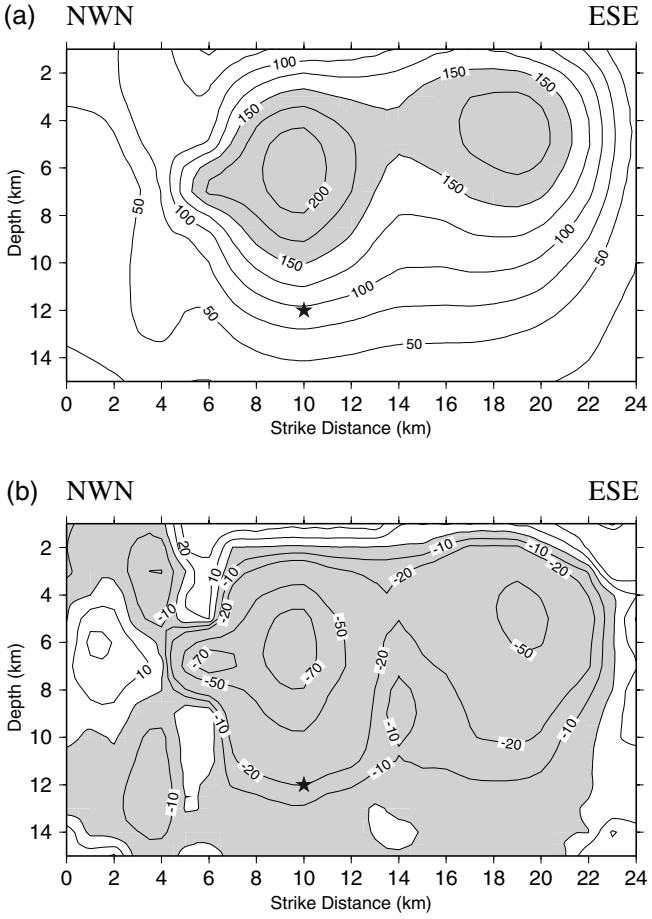

Figure 8. Spatial distribution of (a) slip (Yagi's final model) and (b) stress change for the Tottori earthquake. Shaded and white areas indicate zones of stress decrease and increase, respectively.

served waveform data, and V_{av} is the slip-velocity (dD/dt) averaged over T_{cmin}. If we tentatively take the average as a half of its maximum value V_{max}, then

$$D_{cmin} = T_{cmin} V_{max}/2. \quad (4)$$

The observed records have been lowpass filtered applying a fourth-order butterworth filter with a high-cut frequency of 0.5 Hz. This filter still retains amplitude levels of 70% at 0.5 Hz and 25% at 1 Hz, suggesting that the shortest period remaining on the filtered records, T_{cmin}, will be about 1 sec. The maximum slip velocity obtained here ranges from 50 to 150 cm/sec at different locations on the fault. If we use the above expression, the minimum resolvable D_c would be 25 cm to 75 cm, depending on the location of the subfault, which seems to be quite large at points with large slip velocities.

The second step, for the case when its median value of D_c exceeded the above minimum resolvable limit D_{cmin}, is to estimate the probable error of D_c from the breakdown time $T_c = T_b - T_r$. If we use the relation $D_c \sim T_c \Delta\sigma/\rho\beta$, which can be derived from Ohnaka and Yamashita (1989), then,

$$\Delta D_c \sim \Delta T_c(\Delta\sigma/\rho\beta), \quad \text{and} \quad \Delta D_c/D_c = \Delta T_c/T_c \sim \Delta T_c'/T_c' \quad (5)$$

where $\Delta\sigma$ and ρ are the breakdown stress drop and density, respectively, and $T_c' = T_{pv} - T_r$ is the time from the onset to the peak time. As described in the foregoing section for the kinematic waveform inversion, the source time function on each subfault is expanded into 39 sequential, overlapping triangular basis functions, each having a half duration of 0.25 sec with a shift of 0.25 sec and a resampling rate of 0.05 sec, to match the synthetics to the observed waveforms. This procedure yields the slip-velocity functions shown in Figure 9. In this procedure, we estimate a probable error $\Delta T_c'$ to be less than 0.25 + 0.05 = 0.30 sec. Since T_c' in the slip-velocity functions is in the range between 1.2 and 2.6 sec, we find that $\Delta D_c/D_c$ ranges from 12% to 25% or ΔD_c ranges from 6 to 22 cm depending on the location on the fault.

We also made another numerical experiments to check the effects of lowpass filtering of the simulated slip-velocity time functions on the estimate of D_c'. This is made for the case with an initial stress of 22.5 MPa plus a uniform random distribution between +20 MPa and −20 MPa, being subjected to a yield stress of 25 MPa and a prescribed value of D_c = 20 cm over the entire fault. The initial stress was constrained to be less than 95% of the yield stress to prevent rupture initiation from several locations on the fault. Other fault parameters are similar to case 1 in Table 1. This calculation allows a maximum frequency of 3 Hz to be resolved assuming six points per minimum wavelength. The results shown in Figure 12 indicate that the D_c' values estimated on the synthetics for cutoff frequencies of 0.5–3.0 Hz agree with each other within less than 5%. Thus, the above effects are found to be quite small as compared with the other uncertainties.

To estimate the upper bound of D_c, we also constructed the stress–slip relations directly from the slip-velocity functions given in Figure 9, which are consistent with the spatial distribution of the final slip and static stress changes shown in Figure 8. To do this, the stress time functions were calculated by convolving the kernel involved in equation (7) in Fukuyama and Madariaga (1998) with the given slip-velocity functions. Figure 13 depicts the calculated stress and slip time histories on all subfaults, where the slip-velocity functions are the same as shown in Figure 9. Figure 14a shows the time histories on subfault b, and Figure 14b gives the stress–slip relation obtained in this case. This relation may be regarded as an apparent slip-weakening behavior, from which we see that the slip-weakening distance could be as long as 1.6 m. It is possible, however, that the stress time function might be somewhat elongated due to the finite grid size and time increment used here. This artificial effect has

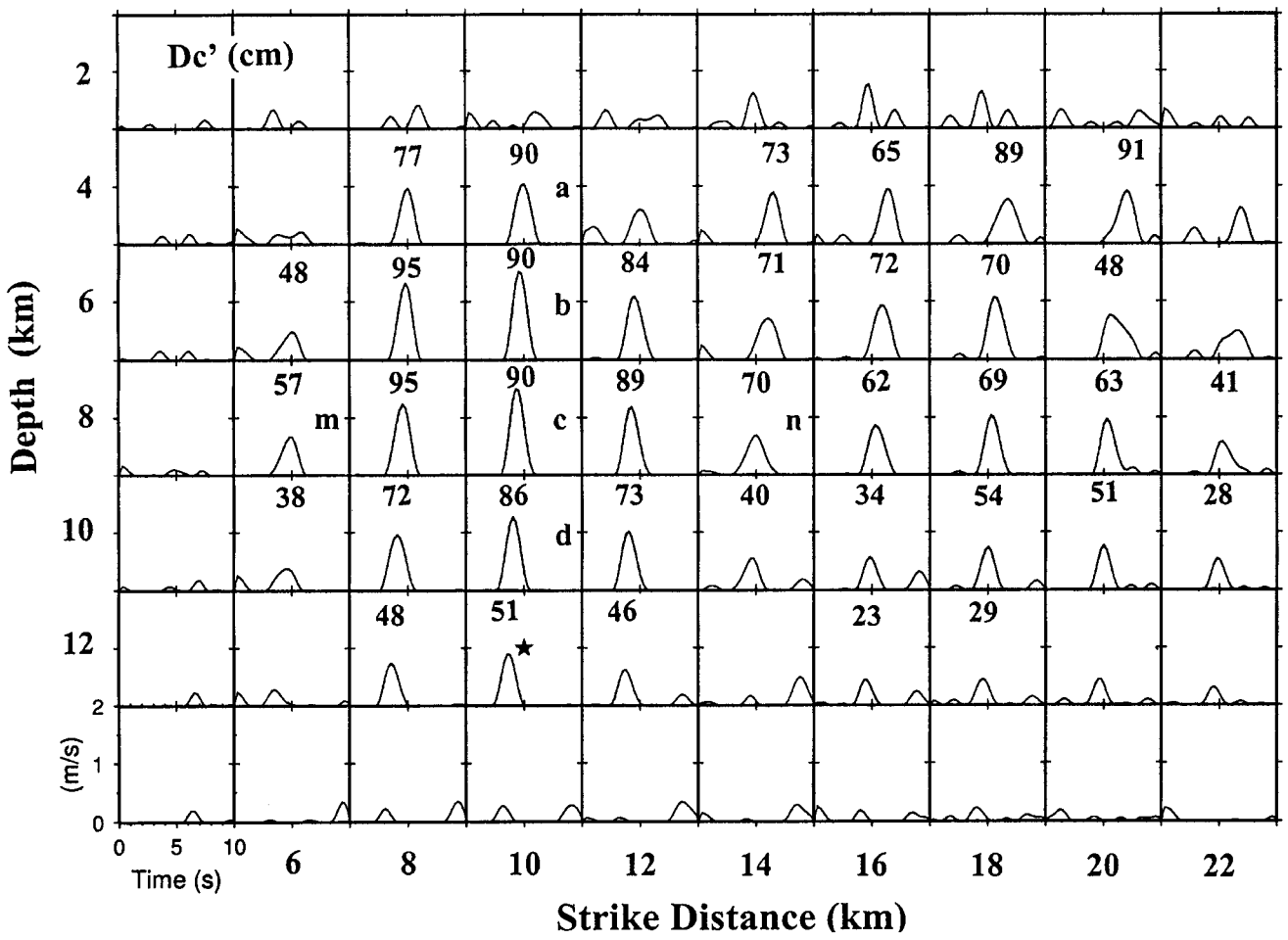

Figure 9. Slip-velocity functions on the subfaults of the segment FD2 for Yagi's final model of the Tottori earthquake. The numerals at the top on each subfault indicate D_c' (in cm) integrated from the slip-velocity functions. Letters a, b, c, d, m, and n denote the indices of the subfaults.

been shown by Ide and Takeo (1997) from their resolution analysis, which performed a similar inversion of synthetic seismograms generated from instantaneous stress drop ($D_c = 0$), with the same basis function and bandpass filtering as in the actual analysis. Their results suggest that the actual slip-weakening distance would be obtained only if this possible artificial effect was corrected. Thus, the slip-weakening distance seen from Figure 14b could be regarded as the upper bound of its actual value, which provides another constraint on D_c.

Spatial Distribution of D_c

The D_c values estimated above are plotted with the minimum resolvable limit and probable errors versus the local maximum slip in Figure 15. In most cases, D_c with large error bars for ΔD_c appears to be somewhat above the minimum resolvable limit D_{cmin}. If this is the case, it appears that the median value of D_c increases with the local maximum slip on each subfault, which tends to fall in the range $0.27 < D_c/D_{max} < 0.56$. However, if the estimates of T_{cmin} and the average slip-velocity are somewhat larger than assumed here, the above trend would become quite marginal.

Taking these uncertainties both in kinematic and dynamic calculations into consideration, we tentatively divide the estimated slip-weakening distance D_c into four ranges. Figure 16 shows the distribution of the estimated ranges of D_c values on the main part of the fault. For some of the peripheral subfaults, the estimated values may be less reliable due to small peak slip velocities or shapes of the slip-velocity functions contaminated by spurious oscillations. Also in some subfaults closer to the east-southeast fault edge, our technique does not apply because of negative stress drop (stress increase), and these subfaults are therefore excluded in Figure 16. From Figure 16, we see that D_c values larger than 80 cm are distributed on the subfaults in the strike direction between 8 and 12 km at depths between 4 and 10 km and at distances between 18 and 20 km at a depth around 4 km. The zones of smaller D_c values between 40 and 60 cm are located not only near the hypocenter but also around the zones with larger values of D_c. This pattern does not

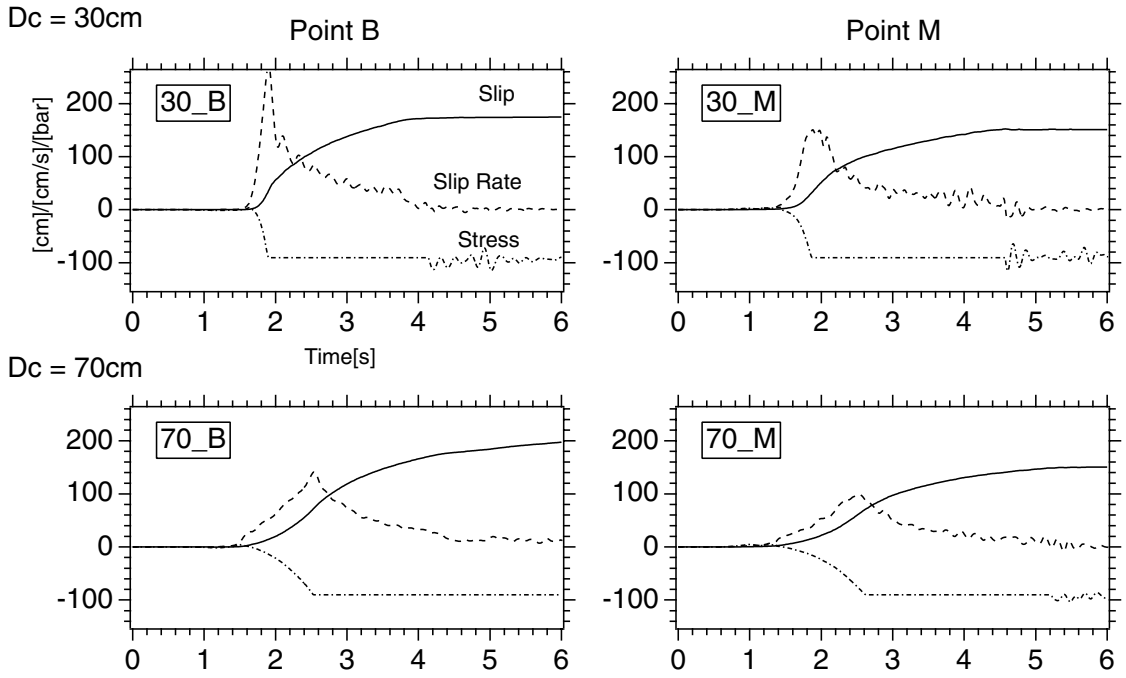

Figure 10. Time histories of stress, slip, and slip velocity at two selected points B(b) and M(m), calculated from the dynamic rupture for prescribed values of D_c = 30 cm and D_c = 70 cm.

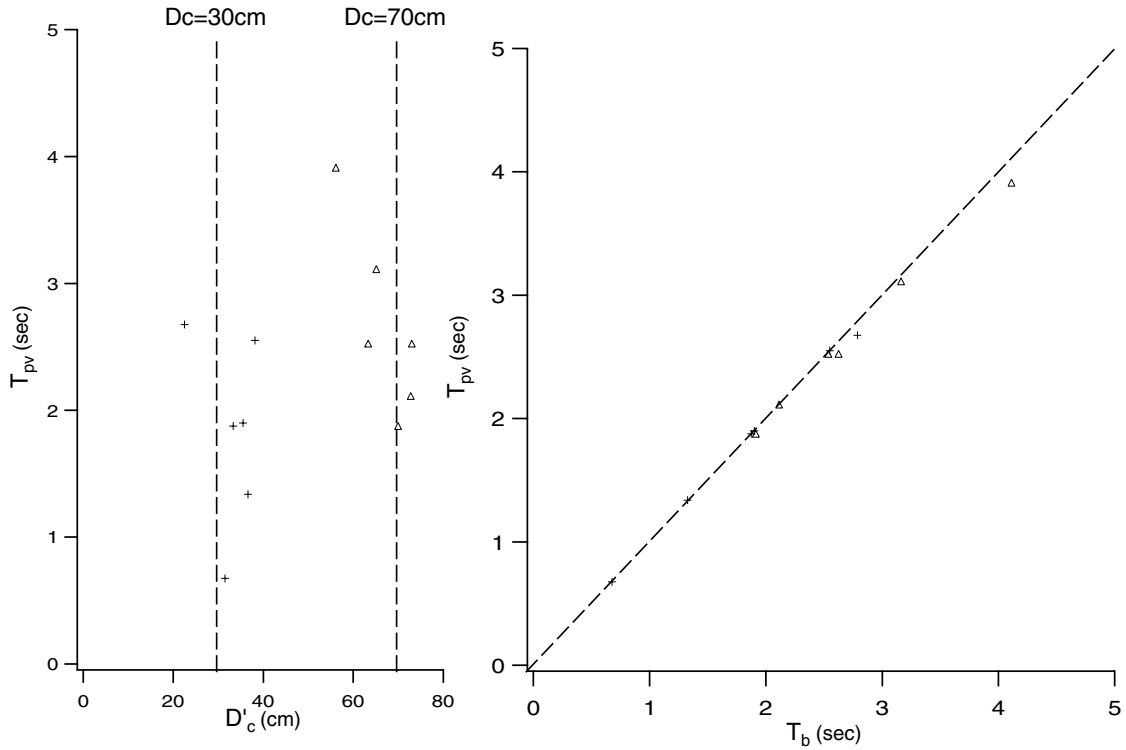

Figure 11. Relation between T_{pv} and T_b (right) and D_c' at T_{pv} (left) for the case shown in Figure 10. T_b and T_{pv} are measured from the origin time at the rupture starting point.

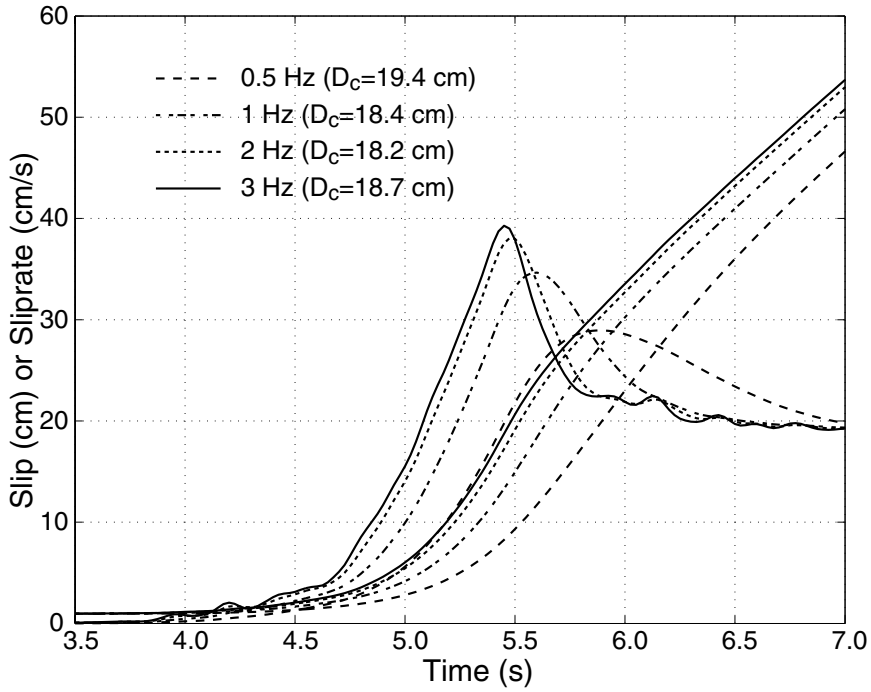

Figure 12. Effect of low-pass filtering of the simulated slip-velocity and slip functions on the estimate of D_c' for a prescribed value of $D_c = 20$ cm. The five different curves correspond to the cases of using cutoff frequencies of 0.5, 1, 2, and 3 Hz.

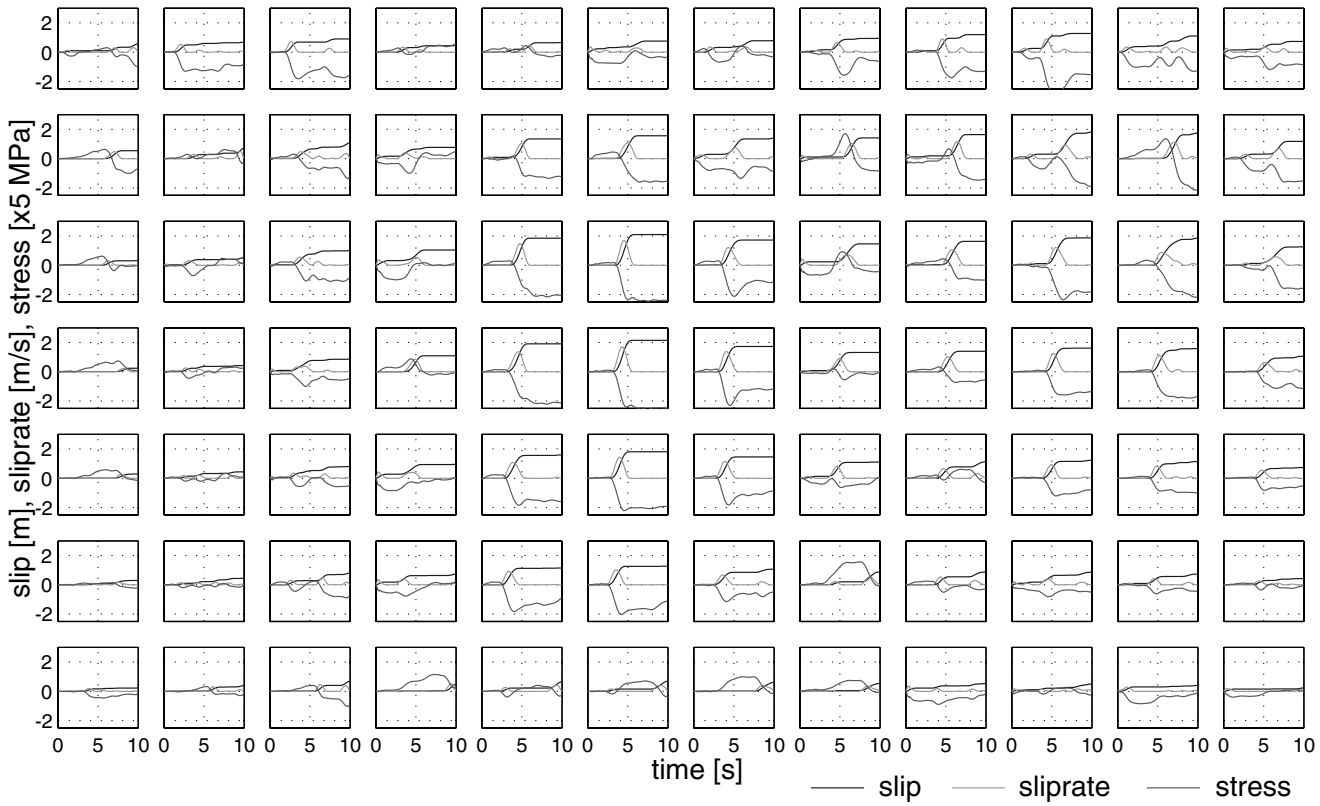

Figure 13. Time histories of stress, slip, and slip velocity on all subfaults, calculated from Yagi's (2001) slip-velocity time functions shown in Figure 9.

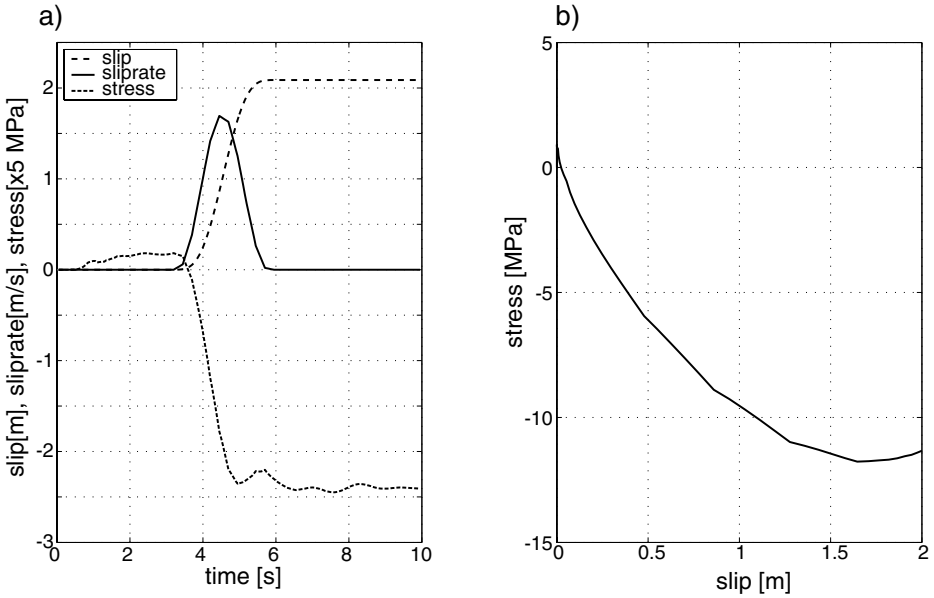

Figure 14. (a) Same as Figure 13 at point b, (b) apparent slip-weakening relation in (a).

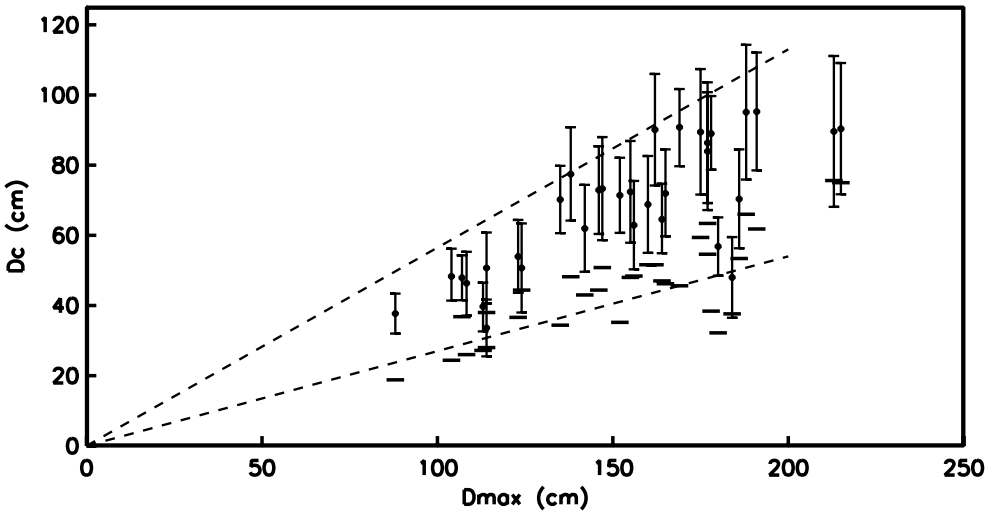

Figure 15. The estimated D_c values with their minimum resolvable limit (thick horizontal bars) and probable errors (thin vertical lines) plotted versus the local maximum slip on all subfaults. The two dashed lines depict the upper and lower ranges of data $D_c = 0.56\ D_{max}$ (upper) and $D_c = 0.27\ D_{max}$ (lower).

necessarily indicate larger D_c at shallow fault sections nor smaller D_c at deeper fault sections, but rather a spatially heterogeneous distribution.

The 1995 Kobe Earthquake

Now, we compare the results for the 2000 Tottori earthquake with those for the 1995 Kobe earthquake (M_w 7.2). The mainshock of the Kobe earthquake was located at 34.61° N and 135.04° E at a depth of 14.3 km (JMA). All the CMT solutions obtained by different institutions indicate a strike-slip mechanism with nearly vertical nodal planes, one of which is parallel and consistent with the direction of lineation of the aftershock distribution. The earthquake was recorded at 18 JMA stations located within 150 km from the epicenter. Ide and Takeo (1997) performed kinematic waveform inversion of 45 displacement seismograms integrated from the recorded accelerograms, which have been band-pass-filtered from 0.025 to 0.5 Hz, to obtain a slip distribution over the fault. The inversion was made for the nearly vertical fault with a dimension of 50 km × 20 km, which was divided into 20 × 8 subfaults with a size of 2.5 km × 2.5 km. The source time function used by Ide and Takeo (1997) is the superposition of six triangles, each with a half duration of 0.6 sec at a time interval of 0.2 sec.

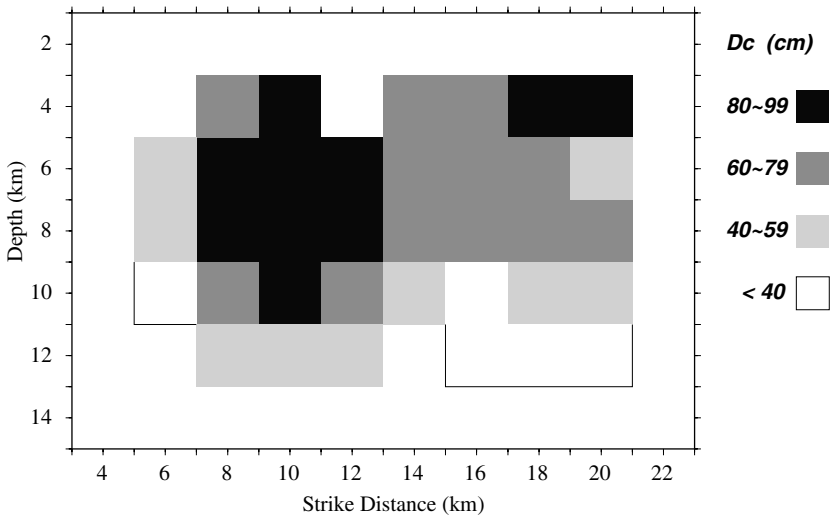

Figure 16. Spatial distribution of the estimated D_c values on the main part of the Tottori earthquake fault, which are tentatively classified into four ranges.

Figure 17 reproduces the spatial distribution of slip and the slip-velocity functions at 10 selected points (a–j) in the shallow fault section, at depths near the hypocenter, and in the deeper part (Ide and Takeo, 1997). We apply our method to these slip-velocity functions to obtain approximate estimates of D_c. For this purpose, we integrate the slip-velocity functions from the arrival time of rupture (all reduced to the origin time) to the time of peak slip-velocity, providing D_c' at time T_{pv}. The calculated values of D_c' are listed at the left top of each point. Three points—d, g, and j—have been excluded because of somewhat noisy shapes of their slip-velocity functions. We find that D_c' at four points—e, f, h, and i—in the deeper fault section are in the range between 40 and 50 cm and that point b in the shallow part yields $D_c' = 90$ cm whereas D_c' at two points a and c ranges between 50 and 60 cm. We did not correct D_c/D_c' for these values from dynamic rupture calculations. From equations (4) and (5) and the observed peak slip-velocities, however, we expect that the minimum resolvable D_c' will be about 25 cm and that the probable error of the D_c' values will be in the range between 25% and 40% considering the duration and time interval of the source time function used in their waveform inversion. On the other hand, the D_c values estimated by Ide and Takeo (1997) from the stress-slip relation should be regarded as the upper bound of their real values because of resolution problems due to the limited grid size and time increment (Ide and Takeo, 1997). The above values estimated here are almost all consistent with those for the Tottori earthquake fault. While smaller values can be found in the deeper fault section as have been stated by Ide and Takeo (1997), all seven values appear spatially variable rather than depth dependent, and a fraction of the local maximum slip. This pattern is also consistent with the case of the Tottori earthquake.

Discussion

Our numerical calculations and discussions are entirely based on the simple slip-weakening model given by Andrews (1976a, b), in which the shear stress decreases linearly with ongoing slip up to the critical weakening slip D_c. However, actual slip-weakening behavior could be different from this idealized case. Actually, Ida (1972), Ohnaka and Yamashita (1989), Matu'ura *et al.* (1992), and Campillo *et al.* (2001) presented somewhat different slip-weakening laws based either on theoretical considerations or on laboratory experiments. Fukuyama *et al.* (2002) used numerical calculations of dynamic rupture, assuming five different types of slip-weakening friction with the same fracture energy G, to investigate the effect of possible differences in the stress change behavior on the relations $T_b \sim T_{pv}$ and $D_c' \sim D_c$. The results show that for the cases of sharp stress drop around T_b, the deviations of D_c' from the prescribed value of D_c, $(D_c' - D_c)/D_c$, are mostly within 20% at a number of points on the fault, but that the cases with very gentle decrease of stress yield quite large deviations sometimes even up to 50%. For more details, see Fukuyama *et al.* (2002). The large deviations in some cases impose another limitation in applying the present technique to estimate the slip-weakening distance D_c from the observed time of peak slip-velocity T_{pv} on the fault.

All the uncertainties described previously, including the limited frequency resolution of the observed waveforms and probable time errors in the slip-velocity functions obtained from kinematic inversion, deviations of T_{pv} from T_b in dynamic rupture, and the possibility of different types of slip-weakening behaviors, which could reach a factor of about 2 if all combined, preclude exact estimates of the slip-weakening distance. Accordingly, the D_c values estimated here are limited by the bandwidth of frequency between 0.05 and 0.5 Hz and are hence constrained to be between the lowest resolvable limit and the upper bound of their real values. This means that any D_c values less than the minimum resolvable limit, if present, have not been resolved in this study. Moreover, for very sharp initiation of the slip-velocity functions similar to that for a Kostrov-type crack model with $D_c \sim 0$ assumed in the 1984 Morgan Hill, California, earth-

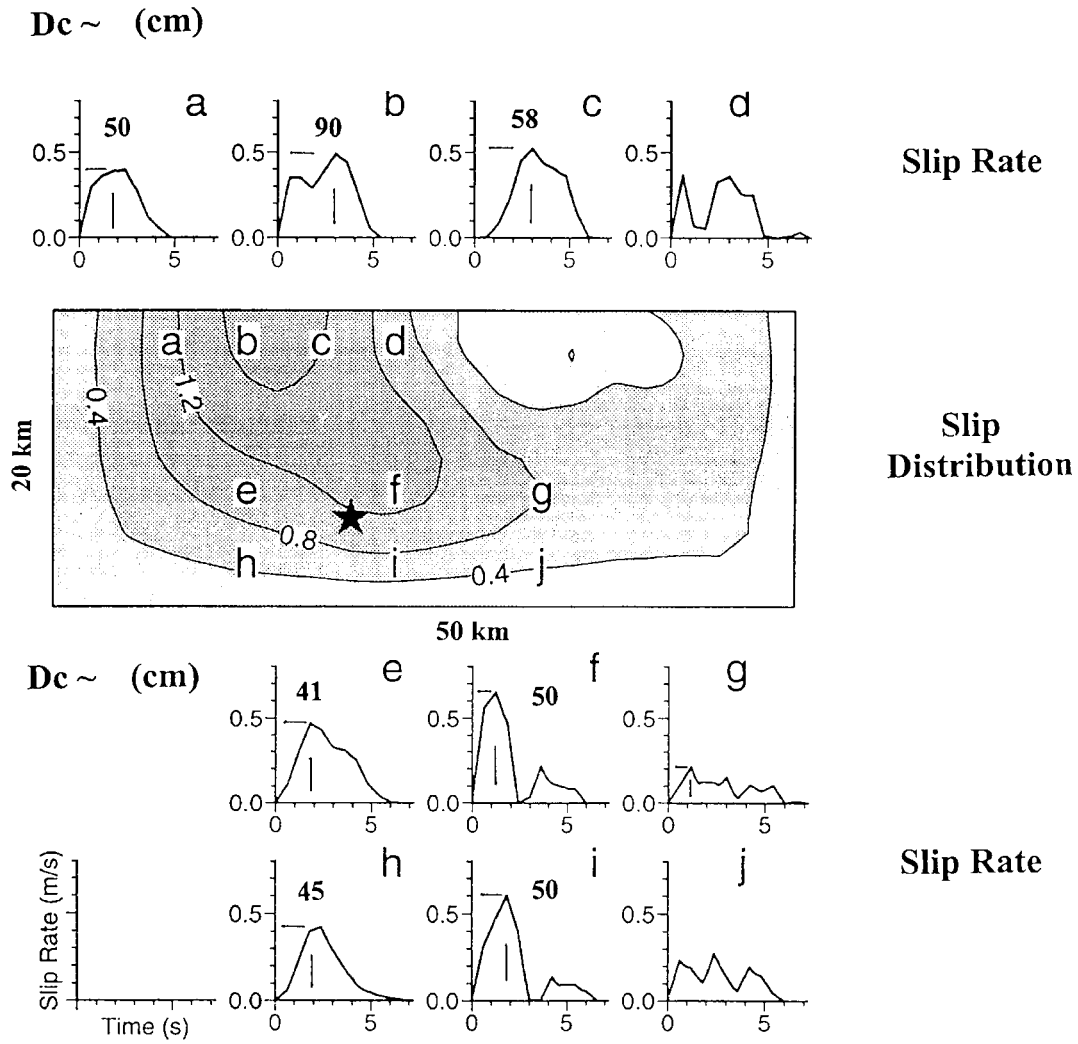

Figure 17. Slip distribution and slip-velocity functions at selected points on the fault for the 1995 Kobe earthquake (Ide and Takeo, 1997). The numerals at the upper left corner indicate D_c' estimated from the slip-velocity functions. Modified, with permission from American Geophysical Union, from figure 4 on p. 27,384 of Ide and Takeo (1997). (Copyright 1997 by the American Geophysical Union.)

quake (Beroza and Spudich, 1988; Beroza and Mikumo, 1996), D_c cannot be resolved by the present technique. This also suggests that our method may not be applicable for much smaller earthquakes with possibly very small D_c values, unless much higher frequency band is used for the analysis.

Now, we discuss other dynamic parameters that might be roughly estimated from our calculations. For the Tottori earthquake fault, the actual breakdown time of stress T_c is estimated from 1.2 to 2.6 sec except at a few points. For the Kobe earthquake, on the other hand, T_c (not corrected) ranges between 1.3 and 3.0 sec, which is slightly longer than for the case of the Tottori earthquake. This minor difference may not be important in view of the limitations of the present technique. The strength excess $\sigma_y - \sigma_0$ may be estimated from dynamic rupture calculations when the rupture arrival time at each point on the fault is specified (Miyatake, 1992; Mikumo and Miyatake, 1995). Although T_r has been estimated within an error of 0.25 sec from the kinematic inversion, the rupture arrival times expected from a fixed velocity of 0.7β for each layer are imposed, instead, in this specific case. For the Tottori earthquake, the strength excess is found to be between 1.5 and 5.0 MPa, although these values may not be well resolved because of the grid spacing used in the numerical calculations. The breakdown stress drop $\sigma_y - \sigma_f = (\sigma_y - \sigma_0) + (\sigma_0 - \sigma_f)$ in the zone of maximum dynamic stress drop is about 11 MPa. By combining the already estimated slip-weakening distance D_c with the breakdown stress drop, the fracture energy $G = (\sigma_y - \sigma_f) D_c/2$ for this zone is found to be on the order of 5 MJ/m^2. This is the same order of magnitude as found in the Morgan Hill (Beroza and Spudich, 1988) and the 1992 Landers (Olsen *et al.*, 1997),

California, earthquakes. All these estimates are obtained from Yagi's (2001) kinematic slip model. It is possible that these values and the spatial distribution of D_c could be slightly different if we refer to other slip models (e.g., Fukuyama and Dreger, 2001; Iwata and Sekiguchi, 2001).

From the results of waveform inversion, Ide and Takeo (1997) found that the slip-weakening distance D_c for the shallow part of the fault is larger than that for the deeper fault sections in the Kobe earthquake. Scholz (1988) has suggested that long-wavelength aperture involved in near-surface rock materials start to close with increasing depth, which makes the slip-weakening distance smaller, while Marone and Kilgore (1993) claimed that thicker fault gouge may cause larger values of D_c in the shallow crust. As shown in Figures 16 and 17, however, the slip-weakening distance for both the Tottori and Kobe earthquakes appears to be slightly dependent on depth but rather spatially variable and more dependent on the local maximum slip, although our estimates have quite large uncertainty as mentioned before. Similar variation has been noticed in the results by Pulido and Irikura (2000) for the 1992 Landers earthquake, although the ratio of D_c to the average slip in their case reaches 70% to 90%, which appears quite large from our point of view. If we take these cases into account, it would follow that physical properties controlling both the slip-weakening distance and the final fault slip could be either the characteristic wavelength of fault roughness (Ohnaka and Shen, 1999) or the thickness of fault gouge layer (Marone and Kilgore, 1993), in addition to the stress distribution on the fault.

The possibility of scale effects of the slip-weakening distance with earthquake size has not been resolved in the present study because we have dealt only with two strike-slip earthquakes with a similar magnitude and a similar mechanism. However, from the apparent slip dependence of the slip-weakening distance shown in Figure 15, if it actually exceeds the lowest resolvable limit, it could be speculated that D_c on faults of smaller-size earthquakes, such as aftershocks on part of the same fault, might be smaller because of smaller final slip. If this is the case, the values of D_c appear to be distributed indicating a fractal-like structure of the roughness of the fault surface. It has been shown by laboratory experiments (Okubo and Dieterich, 1984; Ohnaka and Shen, 1999) that the slip-weakening distance increases with increased fault roughness. Surveys of natural faults (Scholz and Aviles, 1986; Power *et al.*, 1987) also suggested that the topography or roughness of fault surfaces is nearly fractal and hence that the slip-weakening distance controlled by the fault roughness is expected to scale with slip. If so, smaller earthquakes with smaller D_c could also nucleate on the same fault for the same order of dynamic stress drop, as is clear from equation (3) (Day, 1982). This observation also suggests that D_c/D_{max} may be roughly the seismic efficiency (i.e., the ratio of the seismic wave radiation energy to the total energy including the fracture energy) (H. Kanamori, personal comm., 2002). To address these problems, future efforts should apply the present approach to smaller-magnitude earthquakes in the continental crust and also to extremely large thrust earthquakes in subduction zones, taking into account the broadband frequency range of seismic observations.

Finally, the approach described here could also be applied to near-fault strong-motion records, assuming that the strike-parallel slip-velocity and displacement waveforms are approximate expressions of the source time functions on the fault (Olsen *et al.*, 2002).

Conclusions

We present a new approach to estimate the slip-weakening distance on earthquake faults from the slip-velocity functions obtained from inversion of strong-motion records, independently from the estimate of the fracture energy or radiated seismic energy. The approach provides a physically based relation between the breakdown time of shear stress T_b, the time of peak slip-velocity T_{pv}, and the slip-weakening slip D_c, through dynamic rupture calculations using a simple slip-weakening friction law. Numerical calculations show that T_{pv} is well correlated with T_b for faults even with heterogeneous stress-drop distributions, except at points in front of strong barriers and near the edges of the fault.

The aforementioned method has been applied to two recent, strike-slip earthquakes in western Japan: the 2000 Tottori and the 1995 Kobe earthquakes. By integrating the slip-velocity functions on the vertical fault, which had been obtained from kinematic waveform inversion of strong-motion and teleseismic records, we obtain the slip at time T_{pv} and then correct it for the errors expected from dynamic calculations. We also estimated the lowest resolvable limit, the upper bound, and probable errors of D_c from the slip-velocity functions. We found that the actual stress-breakdown time ranges from 1.2 to 3.0 sec, and the slip-weakening distance D_c estimated in the frequency band between 0.05 and 0.5 Hz ranges between 40 and 90 cm on the two earthquake faults. The fracture energy in the zone of maximum slip for the Tottori earthquake is found to be on the order of 5 MJ/m^2. However, from all uncertainties involved in the kinematic and dynamic calculations, the above estimates are limited to the range between the minimum resolvable limit and the upper bound of their real values. The estimated D_c values do not seem to be necessarily depth dependent but rather spatially heterogeneous and appear to be dependent on the local maximum slip. This possible dependence may be interpreted by the frictional properties of the fault such as the degree of roughness and/or the thickness of gouge layers, in addition to the stress heterogeneities.

Acknowledgments

The senior author greatly benefited from conversations with James R. Rice at an early stage of the present study and wishes to thank Miti Ohnaka, Raul Madariaga, and Hiroo Kanamori for some discussion about the present

topics and their constructive comments. We also thank Paul Spudich, Steve Day, and Michel Bouchon (Associate Editor) for their critical and helpful reviews, which greatly improved our original manuscript. Thanks are extended to Satoshi Ide for permitting us to reproduce one of the diagrams from the Kobe earthquake and also to Shri Krishna Singh and Javier Pacheco for their comments. Miguel A. Santoyo and Arturo Iglesias kindly prepared a few figures and files included in the text. Tomotaka Iwata and Takuro Shibutani provided their preliminary reports on the Tottori earthquake. The present work is based on strong-motion data obtained at the stations operated by National Research Institute for Earth Sciences and Disaster Prevention and Japan Meteorological Agency. This study is partly supported by the CONACyT (Mexico) Project No. 32541-T, for which we thank the assistance by Raul Valenzuela. A part of the calculations were made through supercomputers at the Computer Center of the Universidad Nacional Autonoma de Mexico. The work by Kim B. Olsen was supported by the National Science Foundation, award number EAR-0003275 and the Southern California Earthquake Center (SCEC). The SCEC is funded by National Science Foundation Cooperative Agreement EAR-8920136 and U.S. Geological Survey Cooperative Agreements 14-08-0001-A0899 and 1434-HQ-97AG01718. The SCEC Contribution Number for this article is 696 and the ICS Contribution Number is 498.

References

Aki, K., and A. Papageorgiou (1988). Separation of source and site effects in acceleration power spectra of major California earthquakes, *Proc. 9th World Conf. Earthq. Eng.* **VIII,** 163–165.

Andrews, D. J. (1976a). Rupture propagation with finite stress in antiplane, *J. Geophys. Res.* **81,** 3575–3582.

Andrews, D. J. (1976b). Rupture velocity of plane strain shear cracks, *J. Geophys. Res.* **81,** 5679–5687.

Beroza, G. C., and T. Mikumo (1996). Short slip duration in dynamic rupture in the presence of heterogeneous fault properties, *J. Geophys. Res.* **101,** 22,449–22,460.

Beroza, G. C., and P. Spudich (1988). Linearized inversion for fault rupture behavior: application to the 1984 Morgan Hill, California, earthquake, *J. Geophys. Res.* **93,** 6275–6296.

Campillo, M., P. Favreau, I. R. Ionescu, and C. Voisin (2001). On the effective friction law of a heterogeneous fault, *J. Geophys. Res.* **106,** 16,307–16,322.

Clayton, R., and B. Engquist (1977). Absorbing boundary conditions for acoustic and elastic equations, *Bull. Seism. Soc. Am.* **67,** 1529–1540.

Day, S. M. (1982). Three-dimensional simulation of spontaneous rupture: the effect of nonuniform prestress, *Bull. Seism. Soc. Am.* **72,** 1881–1902.

Day, S. M., G. Yu, and D. J. Wald (1998). Dynamic stress change during earthquake rupture, *Bull. Seism. Soc. Am.* **88,** 512–522.

Dieterich, J. H. (1979). Modeling of rock friction 1: Experimental results and constitutive equations, *J. Geophys. Res.* **84,** 2161–2168.

Dieterich, J. H. (1981). Constitutive properties of faults with simulated gouge, *Geophys. Monograph Am. Geophys. Union* **24,** 103–120.

Dieterich, J. H., and B. Kilgore (1996). Implication of fault constitutive properties for earthquake prediction, *Proc. Natl. Acad. Sci. USA* **93,** 3787–3794.

Ellsworth, W. L., and G. C. Beroza (1995). Seismic evidence for an earthquake nucleation phase, *Science* **268,** 851–855.

Fukuyama, E., and R. Madariaga (1995). Integral equation method for plane crack with arbitrary shape in 3D elastic medium, *Bull. Seism. Soc. Am.* **85,** 614–628.

Fukuyama, E., and R. Madariaga (1998). Rupture dynamics of a planar fault in a 3D elastic medium: rate- and slip-weakening friction, *Bull. Seism. Soc. Am.* **88,** 1–17.

Fukuyama, E., and R. Madariaga (2000). Dynamic propagation and interaction of a rupture front on a planar fault, *Pure Appl. Geophys.* **157,** 1959–1979.

Fukuyama, E., M. Ishida, S. Horiuchi, H. Inoue, S. Hori, S. Sekiguchi, T. Eguchi, A. Kubo, H. Kawai, M. Murakami, S. Yamamoto, and K. Nonomura (2001), NIED seismic moment tensor catalogue January–December, 2000, *Technical Note to the National Institute for Earth Sciences and Disaster Prevention* **217,** 1–131.

Fukuyama, E., T. Mikumo, and K. B. Olsen (2003). Estimation of critical slip-weakening distance: its theoretical background, *Bull. Seism. Soc. Am.* (submitted for publication).

Guatteri, M., and P. Spudich (2000). What can strong-motion data tell us about slip-weakening fault-friction laws? *Bull. Seism. Soc. Am.* **90,** 98–116.

Ida, Y. (1972). Cohesive force across the tip of a longitudinal shear crack and Griffith's specific surface energy, *J. Geophys. Res.* **84,** 3796–3805.

Ide, S., and M. Takeo (1997). Determination of constitutive relations of fault slip based on seismic wave analysis, *J. Geophys. Res.* **102,** 27,379–27,391.

Iwata, T., and H. Sekiguchi (2001). Inferences of earthquake rupture process from strong-motion records, presented at the Symposium for Strong-Motion Network.

Kato, N., and T. E. Tullis (2001). A composite rate- and state-dependent law for rock friction, *Geophys. Res. Lett.* **28,** 1103–1106.

Kikuchi, M., and H. Kanamori (1991). Inversion of complex body waves III, *Bull. Seism. Soc. Am.* **81,** 2335–2350.

Kinoshita, S. (1998). Kyoshin Net (K-NET), *Seism. Res. Lett.* **69,** 309–332.

Koketsu, K. (1985). The reflectivity method for synthetic near-field seismograms, *J. Phys. Earth* **33,** 121–131.

Levander, A. (1988). Fourth-order finite difference P-SV seismograms, *Geophysics* **53,** 1425–1436.

Madariaga, R. (1976). Dynamics of an expanding circular fault, *Bull. Seism. Soc. Am.* **66,** 639–667.

Madariaga, R., and K. B. Olsen (2000). Criticality of rupture dynamics in 3-D, *Pure Appl. Geophys.* **157,** 1981–2001.

Madariaga, R., K. B. Olsen, and R. Archuleta (1998). Modeling dynamic rupture in a 3D earthquake fault model, *Bull. Seism. Soc. Am.* **88,** 1182–1197.

Marone, C., and B. Kilgore (1993). Scaling of the critical slip distance for seismic faulting with shear strain in fault zones, *Nature* **362,** 618–621.

Matsu'ura, M., H. Kataoka, and B. Shibazaki (1992). Slip-dependent friction law and nucleation processes in earthquake rupture, *Tectonophysics* **211,** 135–148.

Mikumo, T., and T. Miyatake (1995). Heterogeneous distribution of dynamic stress drop and relative fault strength recovered from the results of waveform inversion: 1984 Morgan Hill, California, earthquake, *Bull. Seism. Soc. Am.* **85,** 178–193.

Mikumo, T., K. Hirahara, and T. Miyatake (1987). Dynamical fault rupture processes in heterogeneous media, *Tectonophysics* **144,** 19–36.

Miyatake, T. (1980). Numerical simulation of earthquake source process by a three-dimensional crack model. I. Rupture process, *J. Phys. Earth* **28,** 565–598.

Miyatake, T. (1992). Reconstruction of dynamic rupture process of an earthquake with constraints of kinematic parameters, *Geophys. Res. Lett.* **19,** 349–352.

Ohnaka, M. (1996). Nonuniformity of the constitutive parameters for shear rupture and quasistaic nucleation to dynamic rupture: a physical model of earthquake generation processes, *Proc. Natl. Acad. Sci. USA* **93,** 3795–3802.

Ohnaka, M. (2000). A physical scaling relation between the size of an earthquake and its nucleation zone size, *Pure Appl. Geophys.* **157,** 2259–2282.

Ohnaka, M., and Y. Kuwahara (1990). Characteristic features of local breakdown near a crack-tip in the transition zone from nucleation to unstable rupture during stick-slip shear failure, *Tectonophysics* **175,** 197–220.

Ohnaka, M., and L-f. Shen (1999). Scaling of the shear rupture process from nucleation to dynamic propagation: Implication of geometric irregularity of the rupturing surfaces, *J. Geophys. Res.* **104,** 817–844.

Ohnaka, M., and T. Yamashita (1989). A cohesive zone model for dynamic shear faulting based on experimentally inferred constitutive relation and strong-motion source parameters, *J. Geophys. Res.* **94,** 4089–4104.

Ohnaka, M., Y. Kuwahara, and K. Yamamoto (1987). Constitutive relations between dynamic physical parameters near a tip of the propagating slip zone during stick-slip shear failure, *Tectonophysics* **144,** 109–125.

Okubo, P. G., and J. H. Dieterich (1984). Effects of physical fault properties on frictional instabilities produced on simulated faults, *J. Geophys. Res.* **89,** 5817–5827.

Olsen, K. B. (1994). Simulation of three-dimensional wave propagation in the Salt Lake Basin, *Ph.D. Thesis*, University of Utah, 157 pp.

Olsen, K. B., and R. Archuleta (1996). Three-dimensional simulation of earthquakes on the Los Angeles Basin fault system, *Bull. Seism. Soc. Am.* **86,** 575–596.

Olsen, K. B., R. Archuleta, and J. Matarese (1995). Three-dimensional simulation of a magnitude 7.75 earthquake on the San Andreas fault, *Science* **270,** 1628–1632.

Olsen, K. B., E. Fukuyama, and T. Mikumo (2002). Direct measurement of slip-weakening friction from near-fault strong motion data, in *Proc. 3rd ACES Workshop*, Hawaii (in press).

Olsen, K. B., R. Madariaga, and R. J. Archuleta (1997). Three-dimensional dynamic simulation of the 1992 Landers earthquake, *Science* **278,** 834–838.

Palmer, A. C., and J. R. Rice (1973). The growth of slip surfaces in the progressive failure of over-consolidated clay, *Proc. R. Soc. London A* **332,** 527–548.

Papageorgiou, A. S., and K. Aki (1983). A specific barrier model for the quantitative description of inhomogeneous faulting and the prediction of strong-ground motion. II. Applications of the model, *Bull. Seism. Soc. Am.* **73,** 953–978.

Peyrat, S., K. B. Olsen, and R. Madariaga (2001). Dynamic modeling of the 1992 Landers earthquake, *J. Geophys. Res.* **106,** 26,467–26,482.

Power, W. L., T. E. Tullis, S. R. Brown, G. N. Boitnott, and C. H. Scholz (1987). Roughness of natural fault surfaces, *Geophys. Res. Lett.* **14,** 29–32.

Pulido, N., and K. Irikura (2000). Estimation of dynamic rupture parameters from the radiated seismic energy and apparent stress, *Geophys. Res. Lett.* **27,** 3945–3948.

Ruina, A. (1983). Slip instability and state variable friction laws, *J. Geophys. Res.* **88,** 10,359–10,370.

Scholz, C. (1988). The critical slip distance for seismic faulting, *Nature* **336,** 761–763.

Scholz, C., and C. A. Aviles (1986). The fractal geometry of faults and faulting, in *Earthquake Source Mechanics*, S. Das, J. Boatwright, and C. H. Scholz, (Editors) American Geophysical Union Monograph 37, Maurice Ewing Vol. 6, 147–155.

Shibazaki, B., and M. Matsu'ura (1992). Spontaneous processes for nucleation, dynamic propagation, and stop of earthquake rupture, *Geophys. Res. Lett.* **19,** 1189–1192.

Shibazaki, B., and M. Matsu'ura (1998). Transition process from nucleation to high-speed rupture propagation: scaling from stick-slip experiments to natural earthquakes, *Geophys. J. Int.* **132,** 14–30.

Shibutani, T., S. Nakao, R. Nishida, F. Takeuchi, K. Watanabe, and Y. Umeda (2002). Swarm-like seismic activities in 1989, 1990 and 1997 which preceded the 2000 Western Tottori earthquake, *Earth Planets Space* **54,** 831–845.

Tullis, T. E. (1996). Rock friction and its implications for earthquake prediction examined via models of Parkfield earthquakes, *Proc. Natl. Acad. Sci. USA* **93,** 3803–3810.

Virieux, J. (1986). P-SV wave propagation in heterogeneous media: velocity-stress finite difference method, *Geophysics* **51,** 889–901.

Yagi, Y. (2001). Source rupture process of the Tottori-ken Seibu earthquake of Oct. 6, 2000, obtained by joint inversion of near-field and teleseismic data, presented at the Meeting of Japan Earth and Planetary Sciences, Tokyo, Japan, May 2001.

Instituto de Geofisica
Universidad Nacional Autonoma de Mexico
Mexico 04510 D.F., Mexico
mikumo@ollin.igeofcu.unam.mx
(T.M.)

Institute for Crustal Studies
University of California, Santa Barbara
Santa Barbara, California 93106-1100
kbolsen@crustal.ucsb.edu
(K.B.O)

National Research Institute for Earth Sciences and Disaster Prevention
Tsukuba, Ibaraki 305-0006, Japan
fuku@bosai.go.jp
(E.F.)

Earthquake Research Institute
University of Tokyo
Tokyo 113-0032, Japan
(Y.Y.)

Manuscript received 4 March 2002.